



Instability of surface-temperature filaments in strain and shear

B. J. Harvey* and M. H. P. Ambaum

University of Reading, Reading, UK

*Correspondence to: B. J. Harvey, Department of Meteorology, University of Reading, PO Box 243, Reading, RG6 6BB, UK. E-mail: b.j.harvey@reading.ac.uk

The effects of uniform straining and shearing on the stability of a surface quasi-geostrophic temperature filament are investigated. Straining is shown to stabilize perturbations for wide filaments but only for a finite time until the filament thins to a critical width, after which some perturbations can grow. No filament can be stabilized in practice, since there are perturbations that can grow large for any strain rate. The optimally growing perturbations, defined as solutions that reach a certain threshold amplitude first, are found numerically for a wide range of parameter values. The radii of the vortices formed through nonlinear roll-up are found to be proportional to θ/s , where θ is the temperature anomaly of the filament and s the strain rate, and are not dependent on the initial size of the filament.

Shearing is shown to reduce the normal-mode growth rates, but it cannot stabilize them completely when there are temperature discontinuities in the basic state; smooth filaments can be stabilized completely by shearing and a simple scaling argument provides the shear rate required. Copyright © 2010 Royal Meteorological Society

Key Words: surface quasi-geostrophic dynamics; stability; turbulence

Received 26 January 2010; Revised 20 April 2010; Accepted 29 April 2010; Published online in Wiley Online Library 16 August 2010

Citation: Harvey BJ, Ambaum MHP. 2010. Instability of surface-temperature filaments in strain and shear. *Q. J. R. Meteorol. Soc.* **136**: 1506–1513. DOI:10.1002/qj.651

1. Introduction

The surface quasi-geostrophic (SQG) equations provide an accurate model for the motion of rapidly rotating stratified fluids near horizontal boundaries. In the atmospheric context, there is a body of work applying the SQG equations to the dynamics of surface-temperature anomalies (Müller, *et al.*, 1989; Schär and Davies, 1990; Ambaum and Athanasiadis, 2007) and also to the dynamics of tropopause-height anomalies (Juckes, 1994, 1995, 1999; Tulloch and Smith, 2006). More recently their application to upper-level ocean dynamics has also been demonstrated (Lapeyre and Klein, 2006).

The model consists of two-dimensional advection of the boundary-temperature field under the assumption of uniform potential vorticity in the fluid interior. The surface streamfunction is related to the surface-temperature field by a Green's function that decays like $1/r$ (see (4) later). This induces a more localized dynamics compared with the more familiar barotropic vorticity equation, which has a Green's

function with a $-\log r$ decay. The $1/r$ Green's function is the same as the full three-dimensional quasi-geostrophic flow, and the SQG system exhibits flavours of three-dimensional flows despite its two-dimensional form (Constantin, *et al.*, 1994).

Here we investigate the striking 'curdling' at small scales that is apparent in many SQG turbulence simulations (Pierrehumbert, *et al.*, 1994; Held, *et al.*, 1995; Juckes, 1995). This curdling is an explanation for the instability of filamentary stratospheric intrusions as well as surface-temperature features. The production and stretching of filamentary structures is a ubiquitous feature of two-dimensional fluid flows, providing a mechanism for the transport of enstrophy to small scales. In the SQG case, however, the filaments appear prone to instability, leading to their break-up and the subsequent formation of smaller-scale vortices. These vortices in turn shed smaller filaments themselves and the process repeats to ever smaller scales. The smaller-scale SQG filaments have larger perturbation growth rates (see below) and therefore this process can

potentially accelerate, resulting in intense activity at small scales on very short time-scales, hence the curdling.

The stability of an isolated SQG temperature filament was studied in detail by Juckes (1995). In this article we investigate the filament instability under typical turbulence conditions by considering separately the effects of external straining and shearing flows. Such flows provide a first-order approximation to the general tendency of the large-scale components of flows to form, stretch, thin and shear smaller-scale filamentary structures.

That external flows can strongly affect fluid dynamic instabilities has long been understood. Dritschel (1989) and Dritschel, *et al.* (1991) study the most basic cases of a barotropic vorticity filament in shear and strain respectively, and we follow a similar methodology in this study. They find that suitably strong shear or strain can completely stabilize vorticity filaments. Other studies have subsequently applied these ideas to the stability of frontal potential vorticity anomalies in the atmosphere (Bishop and Thorpe, 1994; Dacre and Gray, 2006).

Because the SQG system is less familiar than the barotropic system, we briefly outline its structure and the notation we employ in section 2. We then review the basic instability mechanism of SQG filaments in the absence of external flow fields in section 3. The analysis of the straining case is presented in Sections 4–6. In section 4 we consider the instantaneous growth rates of perturbations analytically, while in section 5 we present numerical integrations of the initial-value problem to study the evolution of perturbations in detail. Finally in section 6 we consider an alternative approach to the initial-value problem whereby we suppose perturbations are continually applied to the filament since, as we show, the first perturbation to be applied is not always the first to become large. The analysis of the shear case is more straightforward and is presented in section 7. We present some concluding remarks in section 8.

2. Governing equations

With the atmospheric surface-temperature anomaly application in mind for the choice of notation, we write the SQG system as follows:

$$\frac{D\theta}{Dt} = 0 \quad \text{at } z = 0 \tag{1}$$

$$\text{and } \nabla^2\psi = 0 \quad \text{in } z > 0, \tag{2}$$

where θ is proportional to the potential temperature anomaly and ψ is the geostrophic streamfunction, $D/Dt = \partial/\partial t + u\partial/\partial x + v\partial/\partial y$ is the geostrophic Lagrangian derivative and (2) represents the condition of zero interior PV. The geostrophic variables are given by

$$(u, v, \theta) = (-\psi_y, \psi_x, \psi_z), \tag{3}$$

and u, v and θ are all assumed to decay at large z . Given a surface θ distribution, (2)–(3) then determine all other fields uniquely. For the atmospheric lower boundary application, θ is the potential temperature anomaly scaled by $g/\theta_{00}N$ and therefore has the dimension of a velocity field, z is the vertical coordinate scaled with the Prandtl ratio, N/f , and θ_{00} is a constant background reference temperature.

In the following we suppress the z -dependence of all variables and consider only their surface values. The

inversion of a surface-temperature distribution $\theta(\mathbf{x})$, where $\mathbf{x} = (x, y)$, then takes the form

$$(u, v)(\mathbf{x}) = -\frac{1}{2\pi} \left(-\frac{\partial}{\partial y}, \frac{\partial}{\partial x} \right) \iint \frac{\theta(\mathbf{x}')}{|\mathbf{x} - \mathbf{x}'|} d^2\mathbf{x}', \tag{4}$$

which can be derived by considering the Fourier transform of the full three-dimensional system. For a one-dimensional surface-temperature profile $\theta = \theta(y)$ this inversion reduces to a Hilbert transform,

$$u(y) = -\frac{1}{\pi} \int_{-\infty}^{\infty} \frac{\theta(y')}{y - y'} dy', \quad v = 0. \tag{5}$$

3. Analysis of an isolated filament

Here we briefly outline the stability analysis of an SQG filament in a quiescent background flow. Many of the results were derived by Juckes (1995); the purpose of this review is to introduce notation and define several important parameters used in later sections.

The problem considered is that of a filament of anomalous surface temperature with a ‘top-hat’ profile as illustrated in Figure 1(a):

$$\theta = \Theta(y) \equiv \begin{cases} \theta_0 & \text{for } |y| < L/2, \\ 0 & \text{for } |y| > L/2. \end{cases} \tag{6}$$

The velocity field induced by this temperature anomaly is also sketched in the figure. From (5), it is proportional to the Hilbert transform of the temperature field,

$$u = U(y) = \frac{\theta_0}{\pi} \log \left| \frac{y - L/2}{y + L/2} \right|, \quad v = 0. \tag{7}$$

The logarithmic singularities in the velocity field along the edges of the filament are a generic feature of temperature discontinuities under SQG inversion (Held, *et al.*, 1995). Juckes (1995) shows that despite this singularity the stability characteristics of a slightly smoothed version of this filament are regular in the limit of sharp edges, at least for wave numbers $k \ll \delta L^{-1}$, where δL is the width of the smoothing. We concentrate on the sharp-edge case in the following.

In the sharp-edge limit, the dynamics are governed entirely by the positions of the filament edges. Suppose the edges are perturbed to the new positions $y_1(x, t) = [1/2 + \epsilon\eta_1(x, t)]L$ and $y_2(x, t) = [-1/2 + \epsilon\eta_2(x, t)]L$, where ϵ is a small non-dimensional parameter. Conservation of θ requires the filament edges to be material lines, and so their evolution is given by

$$\frac{\partial \eta_1}{\partial t} = \mathbf{u}(x, y_1 + \delta) \cdot \left(-\frac{\partial \eta_1}{\partial x}, \frac{1}{\epsilon L} \right)^T, \tag{8}$$

$$\frac{\partial \eta_2}{\partial t} = \mathbf{u}(x, y_2 + \delta) \cdot \left(-\frac{\partial \eta_2}{\partial x}, \frac{1}{\epsilon L} \right)^T \tag{9}$$

in the limit $\delta \rightarrow 0$. These equations represent the advection of the boundary by the velocity field at the positions $y = y_1 + \delta$ and $y = y_2 + \delta$ respectively. At these locations the velocity field is finite. In the limit $\delta \rightarrow 0$ the velocity components become large, but the inner products remain finite: the large velocities always run parallel to the edges,

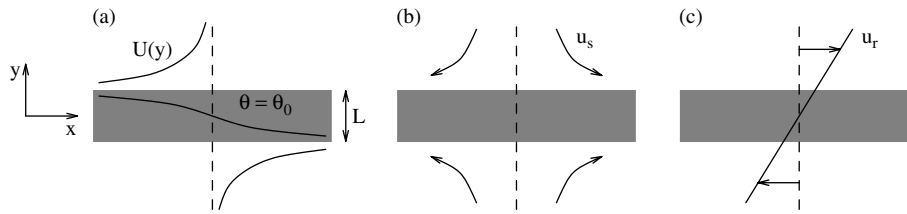


Figure 1. Sketches of (a) the basic-state temperature and velocity fields, (b) the strain flow of (20) and (c) the shear flow of section 7.

leaving evolution of the temperature field on finite time-scales. For a more detailed discussion see Held, *et al.* (1995), Jukes (1995) and Harvey and Ambaum (2010).

Jukes (1995) simplifies the system (8)–(9) by linearizing the velocity field for small ϵ . The dynamics of perturbations on each edge of the filament then consist of a contribution from self-propagation and a contribution from interaction with the opposite edge, a process which can be written succinctly in terms of Fourier components:

$$i \frac{d\hat{\eta}}{dt} = \begin{pmatrix} P(\kappa) & I(\kappa) \\ -I(\kappa) & -P(\kappa) \end{pmatrix} \hat{\eta} \equiv \mathcal{F}\hat{\eta}, \quad (10)$$

where

$$\kappa = kL \quad (11)$$

is the non-dimensional wave number and the Fourier components of the disturbance are defined by $(\eta_1, \eta_2) = \hat{\eta}(t)e^{i\kappa x}$. The propagation (P) and interaction (I) coefficients for the SQG filament problem are given by

$$P(\kappa) = \frac{\theta_0}{\pi L} \kappa (\log \kappa + \gamma - \log 2), \quad (12)$$

$$I(\kappa) = \frac{\theta_0}{\pi L} \kappa K_0(\kappa), \quad (13)$$

where $\gamma = 0.57721 \dots$ is the Euler constant and K_0 is the modified Bessel function of order zero.

The general solution to (10) can be written as

$$\hat{\eta}(t) = \left(\mathcal{I} \cosh \sigma t - \mathcal{F} \frac{i \sinh \sigma t}{\sigma} \right) \hat{\eta}(0), \quad (14)$$

where $\sigma = \sqrt{\det \mathcal{F}} = \sqrt{P^2 - I^2}$ is the normal-mode growth rate and \mathcal{I} is the identity matrix. Note from (12) and (13) that $\sigma \propto \theta_0/L$ and so perturbation growth rates are inversely proportional to the filament width.

To measure the amplification of disturbances we use the r.m.s. wave slope norm which, for a single Fourier mode, is given by

$$\mathcal{N}(t) = \frac{\kappa}{\sqrt{2}} |\hat{\eta}(t)|. \quad (15)$$

This norm represents the size of the dominant nonlinear terms in the governing equations, which typically consist of derivatives, and as such is a useful diagnostic for nonlinear development (Dritschel, *et al.*, 1991). The corresponding norm amplification factor is (taking $|\hat{\eta}(0)| = 1$)

$$\mathcal{A}(t) \equiv \frac{\mathcal{N}(t)}{\mathcal{N}(0)} = |\hat{\eta}(t)|, \quad (16)$$

the rate of change of which can be shown to be given by

$$\frac{d\mathcal{A}}{dt} = -\frac{2}{|\hat{\eta}|} I(\kappa) \Im(\hat{\eta}_1 \hat{\eta}_2^*), \quad (17)$$

where $\Im(\cdot)$ represents the imaginary component of the argument. This growth rate takes a maximal value of $I(\kappa)$ for waves of equal amplitude and a phase difference of $\pi/2$. This is therefore the disturbance configuration that undergoes maximum instantaneous growth under this norm.

Two further quantities of interest are the value of the amplification factor (16) maximized over all initial conditions of a given wave number,

$$\mathcal{A}^*(t) \equiv \max_{\hat{\eta}(0)} [\mathcal{A}(t)], \quad (18)$$

and the corresponding equivalent growth rate

$$\sigma_{\text{eq}}^* = \log[\mathcal{A}^*(t)]/t. \quad (19)$$

Initially (when $\sigma t \ll 1$), $\sigma_{\text{eq}}^* \sim I(\kappa)$ and in the long time limit (when $\sigma t \gg 1$) $\sigma_{\text{eq}}^* \sim \sigma$: the equivalent growth rate collapses on to the normal-mode growth rate in the long time limit. This represents the possibility of transient growth at a rate larger than σ initially, followed by what is effectively normal-mode growth. A full explanation of this process is given by Jukes (1995), who plots σ_{eq}^* (see figure 2b of that study). We have also reproduced the plot in Figure 8a to allow easy comparison with our shearing case of section 7.

4. External strain

We now investigate the effects of external strain on this stability problem. We will demonstrate that straining is a stabilizing process in the sense that all linear perturbations eventually decay when there is an external strain present. However, we will also show that at intermediate times perturbation growth to any specified amplitude can occur. In this sense, the SQG filament cannot be stabilized by strain.

The external strain is written as

$$(u_s, v_s) = s(x, -y), \quad (20)$$

where s is the strain rate. The effect of this flow on the basic state of (6) is to thin the filament exponentially in the y -direction so that at later times its width is given by $L = L_0 e^{-st}$, where L_0 is the width of the filament at $t = 0$. Note that this increases the growth rate of perturbations in the absence of straining which, from (12) and (13), is proportional to θ_0/L .

The straining also has a direct effect on perturbations, which are squashed in the y -direction and stretched in the x -direction. The linear evolution is still given by (10) but

now with time-varying wave numbers, $k = k_0 e^{-st}$, which correspond to

$$\kappa = \kappa_0 e^{-2st}, \tag{21}$$

and the wave-slope norm of (16) becomes

$$\mathcal{A}(t) = e^{-2st} |\hat{\eta}|, \tag{22}$$

where $\hat{\eta}$ represents the Fourier components of both edge perturbations.

We thus see that the strain introduces two competing effects: there is a kinematic decay of perturbations at constant rate $2s$, which is stabilizing, whilst the thinning of the filament causes an exponential increase in the instantaneous perturbation growth rates.

The analytic solution of (14) is not valid for non-zero strain rates, so in sections 5 and 6 we resort to numerical integration to analyze the problem in detail. As a first consideration of the combined effects, however, we consider the instantaneous growth rates of perturbations for which there is a simple analytic result. From (17) and (22) it is clear that the rate of change of \mathcal{A} takes a maximum value of $I(\kappa) - 2s$ when there is straining, and therefore for each strain rate there is a critical filament width above which no perturbations can grow,

$$L = L_c = \max_{\kappa} \left(\frac{\kappa K_0(\kappa)}{2\pi} \right) \frac{\theta_0}{s} \equiv C \frac{\theta_0}{s}, \tag{23}$$

where $C \approx 0.0742$. This maximum value is achieved at non-dimensional wave number $\kappa \approx 0.595$. Note also that in the long time limit, whereby $\kappa \rightarrow 0$, all perturbations will decay at the kinematic rate of $-2s$.

The result of (23) suggests two regimes for the filament. Either $L < L_c$ initially and there are some perturbations that can grow, or else $L > L_c$ initially and all perturbations initially decay. At the later time

$$t = t_c = \frac{1}{s} \log \left(\frac{sL_0}{C\theta_0} \right), \tag{24}$$

where L_0 is the initial filament width, there will be some perturbations that can grow. Therefore instantaneous perturbation growth can occur for any strain rate but only after the filament has thinned to the critical width L_c .

Applying this argument to the initial-value problem, which we study in detail in section 5, we note that the amplitude of a perturbation applied to a wide filament, in the sense that initially $L > L_c$, will have decayed kinematically by the time $t = t_c$ and will therefore be smaller at this time than its initial value. Whether the perturbation can subsequently become large will depend on whether the ensuing period of growth is sufficient to overcome the initial decay. Note also that if the filament was perturbed with a further disturbance of amplitude $\mathcal{A} = 1$ at time $t = t_c$ then this new disturbance would possibly grow large before the initial perturbation, because it would not have undergone an initial decay. We consider this alternative to the initial-value problem in section 6.

Finally, we briefly note the similarity of the result (23) with that of Dritschel, *et al.* (1991) for the barotropic vorticity case: they found that perturbation growth in vorticity filaments is prevented if $s > 0.25q_0$, where q_0 is the filament vorticity. Likewise, the condition of (23) means that perturbation growth in the SQG case is prevented if $s > C\theta_0/L$. The difference here is the factor L which, due to the exponential thinning of the filament, means that the condition cannot be met indefinitely.

5. Initial value problem

We scale time with respect to the constant strain rate, s :

$$T = st, \tag{25}$$

leaving only two non-dimensional parameters in the linear equations, the initial values of L/L_c and $\kappa = kL$. which we write as L_0/L_c and $\kappa_0 = k_0 L_0$ respectively. In addition, the solution depends on the initial structure of the perturbation, $\hat{\eta}(0)$, but here we only consider the maximum amplification, $\mathcal{A}^*(t)$, introduced in (18). Recall that the wave number of each Fourier mode evolves according to (21) so that the full solution is

$$\eta(x, t) = \hat{\eta}(t) \exp(ik_0 e^{-st} x). \tag{26}$$

The maximum amplification, $\mathcal{A}^*(t)$, can be calculated from numerical integrations using the method of Dritschel, *et al.* (1991) as follows. For given values of L_0 and κ_0 , we numerically integrate the system just twice with different initial conditions to obtain linearly independent solutions $\hat{\mu}(t)$ and $\hat{\nu}(t)$. As the equations are linear, any solution $\hat{\eta}(t)$ can be obtained from linear combinations of the form

$$\hat{\eta}(t) = \alpha \hat{\mu}(t) + \beta \hat{\nu}(t), \tag{27}$$

where α and β are complex constants. $\mathcal{A}(t)$ then takes the form

$$\mathcal{A}(t) = e^{-2st} \left[|\alpha|^2 |\hat{\mu}|^2 + |\beta|^2 |\hat{\nu}|^2 + 2\text{Re}(\alpha\beta^* \hat{\mu} \cdot \hat{\nu}^*) \right]^{\frac{1}{2}}, \tag{28}$$

which can be maximized over all α and β . Choosing $\hat{\mu}$ and $\hat{\nu}$ to satisfy $\hat{\mu}(0) \cdot \hat{\nu}^*(0) = 0$ simplifies the expressions, since then $|\hat{\eta}(0)| = 1$ only requires $|\alpha|^2 + |\beta|^2 = 1$ which, combined with the phase invariance of the dynamics, means we can write

$$\alpha = e^{i\gamma} \cos \delta, \tag{29}$$

$$\beta = e^{-i\gamma} \sin \delta, \tag{30}$$

and maximize (28) with respect to the real constants γ and δ . The maximum of \mathcal{A} resulting from this calculation is

$$\mathcal{A}^*(t) = \frac{e^{-2st}}{\sqrt{2}} \left[|\hat{\mu}|^2 + |\hat{\nu}|^2 + \left\{ (|\hat{\nu}|^2 - |\hat{\mu}|^2)^2 + 4|\hat{\mu} \cdot \hat{\nu}^*|^2 \right\}^{\frac{1}{2}} \right]^{\frac{1}{2}}. \tag{31}$$

To simplify the integration numerics, we use alternative variables defined by $(\hat{\lambda}_1, \hat{\lambda}_2) = [\hat{\eta}_1 + \hat{\eta}_2, i(\hat{\eta}_1 - \hat{\eta}_2)]/\sqrt{2}$, as then all the coefficients in (10) are real. The natural choices of $\hat{\lambda}(0) = (1, 0)$ and $(0, 1)$ for the two linearly independent solutions correspond to

$$\hat{\mu}(0) = \frac{1}{\sqrt{2}}(1, 1), \tag{32}$$

$$\hat{\nu}(0) = \frac{i}{\sqrt{2}}(-1, 1), \tag{33}$$

and this is what we use.

The integration scheme used is a second-order semi-implicit scheme. Accuracy is ensured by systematically reducing the time step until convergence is achieved. Integrations have been performed over a wide range of parameter space ($L_0/L_c, \kappa_0$), and we now discuss the results.

As an initial illustration, Figure 2 shows the evolution of \mathcal{A}^* as a function of the scaled time, T , for various parameter values. Panel (a) shows integrations with initial filament width $L_0 = 0.8L_c$ and several initial wave numbers, κ_0 . Panel (b) conversely shows integrations with equal initial wave numbers and a selection of L_0/L_c values. In all simulations the long time behaviour is that of decay at the kinematic rate. In some cases, however, there is intermediate growth prior to this decay. We are interested in the magnitude of this growth and as such we define $\mathcal{A}_{\max}(L_0/L_c, \kappa_0)$ as the maximum value of \mathcal{A}^* achieved throughout the integration period for each pair of parameter values ($L_0/L_c, \kappa_0$).

Figure 3(a) shows \mathcal{A}_{\max} computed for a wide range of ($L_0/L_c, \kappa_0$) values, and the corresponding time at which the maxima occur, i.e. T_{\max} such that $\mathcal{A}^*(T_{\max}) = \mathcal{A}_{\max}$, is shown in Figure 3(b). Note the logarithmic scales in these plots. The parameter values of the integrations in Figure 2 are also shown on the figure, as well as the border between positive and negative initial growth predicted by (23).

There are two features of Figure 3 that we now discuss. The first, and most important, is that for all values of the initial width L_0 there appear to be wave numbers that have large \mathcal{A}_{\max} values and therefore may be unstable in the sense that nonlinear terms may dominate the dynamics and cause the filament to ‘roll up’. The initial wave numbers, κ_0 , of the perturbations that grow large increase with L_0 , as expected, a result of the following combined effects: (1) the intermediate period of growth seen in Figure 2 occurs when $\kappa = \mathcal{O}(1)$ and (2) perturbation growth rates are larger on thinner filaments. Therefore the largest \mathcal{A}_{\max} values are achieved by the largest κ_0 experiments for which the filaments are very thin by the time $\kappa = \mathcal{O}(1)$. Note that, despite this prediction of nonlinear instability at all strain rates, an initial disturbance of any given wave number can be stabilized if a suitably strong strain is applied.

The second feature of Figure 3 is the small wiggle of the contours in panel (a) in the region of $\log \kappa_0 = 0.5$. This is near the border between positive and negative initial growth and it is associated with the non-modal transient evolution of the isolated filament case (see section 3). In this case, small-scale perturbations beyond the short-wave cut-off of normal-mode growth exhibit oscillatory behaviour due to a lack of phase-locking between the edge waves, as can be seen in Figure 8 of this article or figure 2b of Jukes (1995). The wiggle in Figure 3(a) is a manifestation of this behaviour in the straining case, although here the effect is only temporary because the short waves are stretched to a wavelength where phase-locking can occur and the subsequent perturbation growth then dominates.

We now consider an alternative diagnostic from the integrations: the smallest time at which a certain threshold amplitude \mathcal{A}_{th} is achieved, i.e. the first T_{th} such that $\mathcal{A}^*(T_{\text{th}}) = \mathcal{A}_{\text{th}}$. The motivation for this approach is that the amplification factor \mathcal{A} is a measure of the importance of nonlinear terms in the corresponding full nonlinear problem, and as such filament ‘roll up’ may be expected to occur when this reaches some threshold value. Without knowing this value, which will of course depend on the

absolute size of the initial perturbation, we calculate our results for a range of different threshold amplitudes.

Figure 4 shows T_{th} for the cases $\mathcal{A}_{\text{th}} = e^1 = 2.72 \dots$ and $\mathcal{A}_{\text{th}} = e^4 = 54.6 \dots$. The plots show that for each L_0 there is an optimal initial wave number, $\kappa_{\text{opt}}(L_0; \mathcal{A}_{\text{th}})$, that achieves the threshold amplitude first. This is marked on the plots by the dashed lines. Figure 5(a) shows the corresponding optimal times $T_{\text{opt}}(L_0, \mathcal{A}_{\text{th}})$, which are the times at which the optimal wave number perturbations reach the threshold amplitudes, as a function of L_0 . As expected, the $\mathcal{A}_{\text{th}} = 4$ case has larger T_{opt} values than the $\mathcal{A}_{\text{th}} = 1$ case. Also shown, in Figure 5(b), is an estimate of the radii of vortices formed from the instability, $a_{\text{opt}}(L_0, \mathcal{A}_{\text{th}})$. This is defined such that the area of one vortex is equal to the area of filament contained within one wavelength of the optimally growing mode:

$$\pi a_{\text{opt}}^2 = \frac{2\pi}{\kappa_{\text{opt}}(L_0)} L_0^2. \quad (34)$$

Both panels of Figure 5 show a regime change at a certain value of L_0 , which depends on the choice of \mathcal{A}_{th} . A comparison with Figure 4 suggests the interpretation that for small L_0 values perturbations can grow immediately, whereas for large values none of the initially growing perturbations reaches \mathcal{A}_{th} . Instead, the first perturbation to do so is an initially decaying one, which must then overcome the kinematic decay. The result is that for filaments with large L_0 values the resultant vortices are significantly smaller than the initial filament width.

6. Continued perturbations

We next consider a different approach to the problem, that of a filament under continued perturbations. By this we mean a filament that is perturbed at each instant in time during the integration. We still assume that each perturbation evolves independently of the others but expect that, since the quasi-stationary growth rate increases in time, a perturbation applied at time $T = \tau > 0$ may grow and reach the threshold amplitude \mathcal{A}_{th} before a perturbation applied at time $T = 0$.

Note that the evolution of a perturbation applied at $T = \tau$ is equivalent to that of an initial-value problem with initial value of L given by $L_0 e^{-\tau}$, and therefore all the information we require to test this hypothesis is included in the initial-value integrations already performed.

The motivation for the continued perturbation approach comes from the fact that the wave number of the optimally growing modes is often very large. A filament with initial width $L = 3L_c$ has, for $\mathcal{A}_{\text{th}} = e^4$, an optimally growing mode of initial wave number $\kappa_0 \approx e^6$, and this appears to increase for stronger strain rates (see Figure 4). Clearly a consideration of numerical resolution or other diffusive effects may make these modes unrealistic. Further, defining the initial condition of a filament in a turbulent flow is not a well-defined procedure since there is no time $t = 0$. Instead we suppose that the perturbations are generated throughout the straining period by a noisy background velocity field.

To calculate whether a later perturbation can grow to a particular threshold amplitude before an initial perturbation, consider minimizing the sum of waiting until the perturbation release time τ and the subsequent optimal growth time for a filament of width $L_0 e^{-\tau}$, over all possible

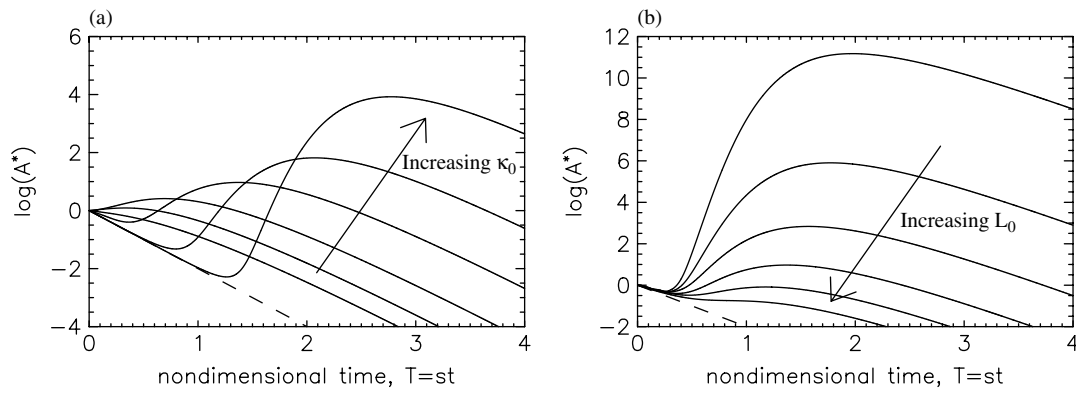


Figure 2. Evolution of $\log[A^*(T)]$ for various parameter values. (a) $L_0 = 0.8L_c$ and $\kappa_0 = \exp[-2, -1, 0, 1, 2, 3]$, as indicated. (b) $L_0 = 0.8L_c \exp[-1.5, -1, -0.5, 0, 0.5, 1]$ and $\kappa_0 = \exp(1)$, as indicated. The dashed lines show the kinematic decay $\log[A^*(T)] = -2T$.

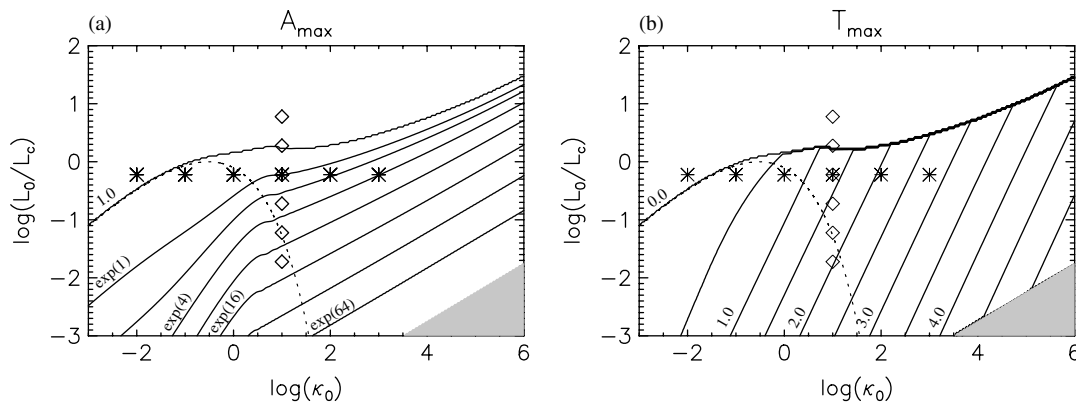


Figure 3. (a) Contours are \mathcal{A}_{\max} , the dotted line represents the boundary between positive and negative initial growth given by $I(\kappa) = 2s$ (see (23) and discussion) and the symbols indicate the parameter values used in Figure 2. (b) Contours are T_{\max} . In both plots the shading indicates regions of parameter space that were not investigated.

release times:

$$T_{cp} = \min_{\tau < T_{opt}(L_0)} [\tau + T_{opt}(L_0 e^{-\tau})]. \quad (35)$$

Either the minimizing τ is zero and it is the initial perturbation that is important or else the minimizing value is positive and it is a perturbation applied later that reaches the threshold amplitude first.

Figure 6(a) shows T_{cp} as a function of L_0 for both $\mathcal{A}_{th} = e^1$ and $\mathcal{A}_{th} = e^4$. For L_0 larger than some critical value, T_{cp} is indeed smaller than T_{opt} , indicating that perturbations applied later are the fastest growing ones. Figure 6(b) shows the corresponding vortex radii of the first perturbations to reach the threshold amplitude, now defined by

$$\pi a_{cp}^2 = \frac{2\pi}{\kappa_{opt}(L_0 e^{-\tau^*})} (L_0 e^{-\tau^*})^2, \quad (36)$$

where τ^* represents the minimizing τ value from (35). This is constant for precisely the same L_0 values and from this we infer the following: if a filament is initially wide, in a sense made precise below, and is continually perturbed, then it has no ‘memory’ and will become unstable only once it has thinned to a critical width that is independent of L_0 . The resultant vortices will have radii proportional to θ_0/s , again independent of how the filament was formed.

The relevant width in this statement refers to the transition in Figure 6 between the regime whereby initial perturbations dominate and the regime whereby later perturbations

dominate, which depends on the value chosen for \mathcal{A}_{th} . Figure 7(a) shows the critical width for various \mathcal{A}_{th} values, and the resulting vortex radii are shown in Figure 7(b).

Both the critical width and the vortex radii values reduce to zero for large \mathcal{A}_{th} . For $\mathcal{A}_{th} = e^4 \approx 54.6$, the theory predicts that instability will occur in a wide filament once the width has reduced to $L \approx 0.3L_c$ and the resultant vortices will have radii $a \approx 0.3L_c$.

7. External shear

In this section we consider the effects of an alternative external flow field, that of a shear flow aligned with the filament as illustrated in Figure 1(c). We find that such a flow can act to stabilize smooth temperature filaments in a manner to be explained, but not the discontinuous ‘top-hat’ profile.

The shear flow is written

$$(u_s, v_s) = r(y, 0), \quad (37)$$

where r is the rate of shear. The analysis of this case is much simpler than the strain case, since the basic state does not evolve in time. The perturbation evolution is still given by (10) with a simple modification to the propagation coefficient,

$$P(\kappa) = \frac{\theta_0}{\pi L} \kappa (\log \kappa + \gamma - \log 2) - \frac{\kappa r}{2}, \quad (38)$$

which represents the modification of the local wave speed due to advection by the shear flow. The analytic solution

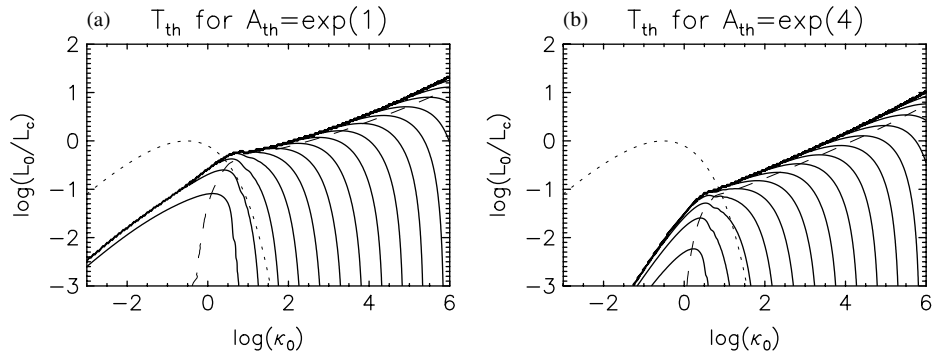


Figure 4. Contoured T_{th} values for threshold amplitudes (a) $\mathcal{A}_{th} = e^1$ and (b) $\mathcal{A}_{th} = e^4$. The dashed line indicates the minimum values, the dotted line is as in Figure 3.

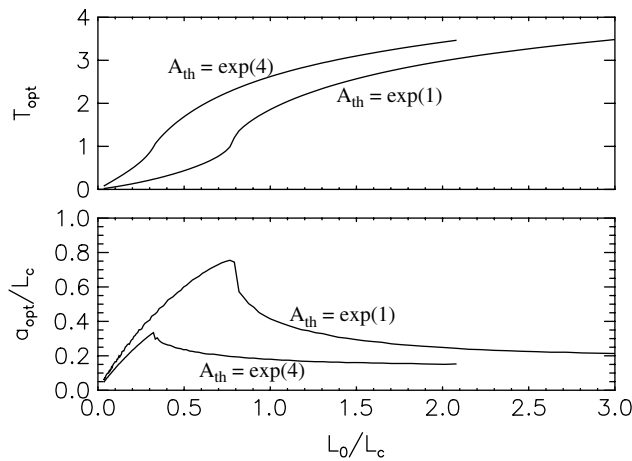


Figure 5. Upper panel: T_{opt} values for the threshold amplitudes $\mathcal{A}_{th} = e^1$ and $\mathcal{A}_{th} = e^4$. Lower panel: a_{opt} values for the same threshold amplitudes, see (34).

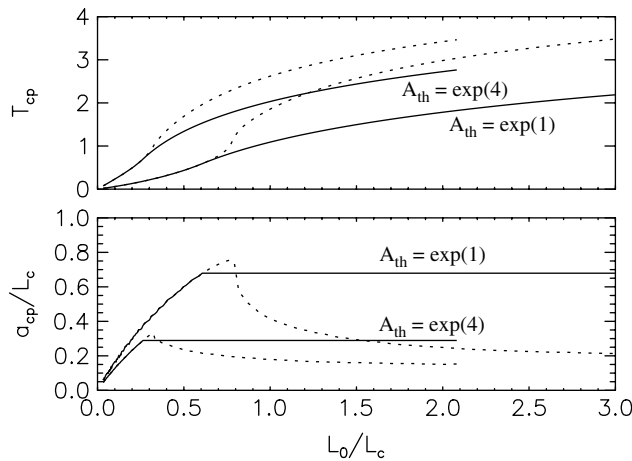


Figure 6. Upper panel: T_{cp} values for the threshold amplitudes $\mathcal{A}_{th} = e^1$ and $\mathcal{A}_{th} = e^4$ (solid lines); dashed lines are T_{opt} (see Figure 5). Lower panel: a_{cp} values for the same threshold amplitudes, see (36).

of (14) also holds with this modification and we plot, in Figure 8, the corresponding equivalent growth rates (see (19)) for various shear values.

The figure shows qualitatively similar behaviour for all of the shear values. The σ_{eq}^* values are all initially equal to $I(\kappa)$ and then collapse on to the normal-mode values. An adverse shear (Figure 8(c)) shifts the unstable normal modes to higher wave numbers, thus reducing the wavelength of the

most unstable perturbations. Likewise, a complementary shear (Figure 8(b)) shifts the unstable normal modes to smaller wave numbers and hence larger wavelengths. The normal-mode growth rate curve always lies below the $I(\kappa)$ curve, which is not affected by the shear. In contrast to the barotropic vorticity case, there is no critical shear value that stabilizes the filament completely; there are always unstable modes, albeit with reduced growth rates. This can be seen from (38): for any value of r there is a κ such that $P(\kappa) = 0$, hence $\sigma = \sqrt{I^2 - P^2}$ is real.

The inability of shear to prevent normal-mode growth of the SQG ‘top-hat’ filament is consistent with a consideration of the Fjortoft condition. Applied to this problem, the condition assures stability provided that the basic-state velocity profile is anti-correlated with the sign of the temperature gradients at each edge of the filament. Clearly (see Figure 1) the velocity singularities at the filament edges prevent this from occurring for any finite shear value.

If, instead, we consider the case of a filament with slightly smoothed edges, then the singularities disappear. Suppose the filament edge is smoothed slightly over a width δL . The peak in the basic-state velocity field will then scale as

$$U_{peak} \sim \frac{\theta_0}{\pi} \log(L/\delta L) \tag{39}$$

and the Fjortoft condition will be met when

$$r \sim \frac{2\theta_0}{\pi L} \log(L/\delta L). \tag{40}$$

Therefore we conclude that smooth temperature filaments can be stabilized by suitably strong shearing, the strength of which is dependent on the filament profile.

8. Conclusions

Straining and shearing tend to inhibit the development of various fluid dynamical instabilities. However, we have shown that straining is unable to stabilize temperature filaments in the surface quasi-geostrophic system, since it acts to thin filaments and thus increase the instantaneous growth rates of perturbations.

Shearing is also unable to stabilize SQG ‘top-hat’ filaments and this is due to the velocity singularities they induce.

For the straining case, our numerical integrations show that the increase in perturbation growth rate is large enough that following the evolution of a single perturbation is not the fastest way to reach large amplitude. Instead, by

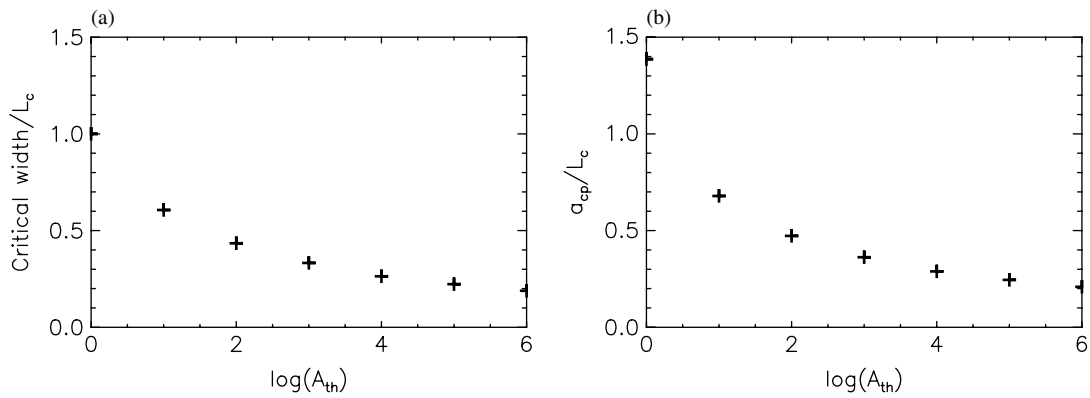


Figure 7. (a) Critical widths versus threshold amplitude, see text. (b) Resultant vortex radii versus threshold amplitude, see text.

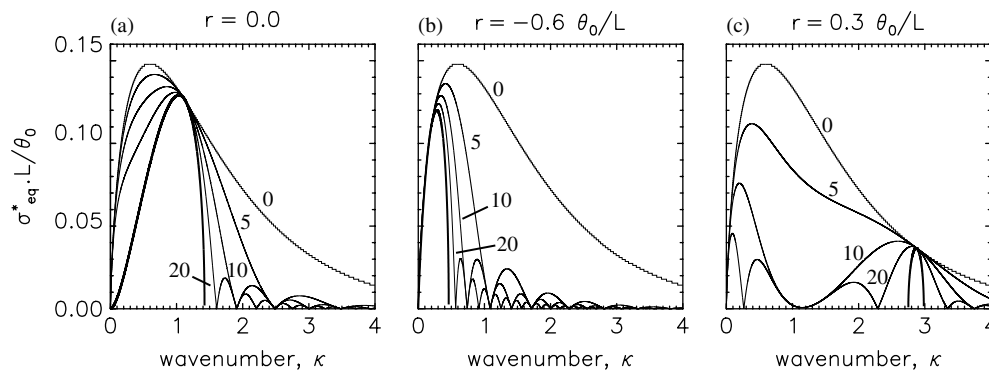


Figure 8. Equivalent growth rate values (see (19)) for rates of shear (a) $r = 0.0$, (b) $r = -0.6\theta_0/L$ and (c) $r = 0.3\theta_0/L$. The times plotted are $t = (0, 5, 10, 20)L/\theta_0$ as indicated and the bold line indicates the normal-mode growth rate.

considering many perturbations applied continuously in time, we found that there is an optimal width for applying a perturbation such that it grows to a given threshold amplitude first. According to this simple theory, the size of the resultant vortices is independent of the previous history of the filament, instead being proportional to θ_0/s , with θ_0 the temperature anomaly of the filament and s the strain rate.

Diffusion will act to smooth the ‘top-hat’ filaments studied here, possibly making the method unsuitable. However, it can be shown analytically that the combined effects of straining and diffusion introduce a critical filament width

$$l_v = \left(\frac{\nu}{s}\right)^{1/2}, \quad (41)$$

where ν is the diffusion coefficient, above which diffusion plays a minor role. We therefore expect filament instability to occur readily if $L_c \gg l_v$, or alternatively if filament amplitudes typically satisfy

$$\theta_0 \gg \frac{\sqrt{\nu s}}{C}, \quad (42)$$

where $C \approx 0.0742$. For filaments satisfying these criteria, diffusion can be ignored.

References

- Ambaum MHP, Athanasiadis PJ. 2007. The response of a uniform horizontal temperature gradient to heating. *J. Atmos. Sci.* **64**: 3708–3716.
- Bishop CH, Thorpe AJ. 1994. Frontal wave stability during moist deformation frontogenesis. Part I: Linear wave dynamics. *J. Atmos. Sci.* **51**: 852–873.
- Constantin P, Majda AJ, Tabak E. 1994. Formation of strong fronts in the 2-D quasigeostrophic thermal active scalar. *Nonlinearity* **7**: 1495–1533.
- Dacre HF, Gray SL. 2006. Life-cycle simulations of shallow frontal waves and the impact of deformation strain. *Q. J. R. Meteorol. Soc.* **132**: 2171–2190.
- Dritschel DG. 1989. On the stabilization of a two-dimensional vortex strip by adverse shear. *J. Fluid Mech.* **206**: 193–221.
- Dritschel DG, Haynes P, Jukes M, Shepherd T. 1991. The stability of two-dimensional vorticity filament under uniform strain. *J. Fluid Mech.* **230**: 647–665.
- Harvey BJ, Ambaum MHP. 2010. Perturbed rankine vortices in surface quasi-geostrophic dynamics. *Geophys. Astrophys. Fluid Dyn.* In press.
- Held IM, Pierrehumbert RT, Garner ST, Swanson KL. 1995. Surface quasi-geostrophic dynamics. *J. Fluid Mech.* **282**: 1–20.
- Jukes M. 1994. Quasigeostrophic dynamics of the tropopause. *J. Atmos. Sci.* **51**: 2756–2768.
- Jukes M. 1995. Instability of surface and upper-tropospheric shear lines. *J. Atmos. Sci.* **52**: 3247–3262.
- Jukes M. 1999. The structure of idealised upper-tropospheric shear lines. *J. Atmos. Sci.* **56**: 2830–2845.
- Lapeyre G, Klein P. 2006. Dynamics of the upper oceanic layers in terms of surface quasigeostrophy theory. *J. Phys. Oceanogr.* **36**: 165–176.
- Müller JC, Davies HC, Schär C. 1989. An unsung mechanism for frontogenesis and cyclogenesis. *J. Atmos. Sci.* **46**: 3664–3672.
- Pierrehumbert RT, Held IM, Swanson KL. 1994. Spectra of local and nonlocal two-dimensional turbulence. *Chaos, Solitons and Fractals* **4**: 1111–1116.
- Schär C, Davies HC. 1990. An instability of mature cold fronts. *J. Atmos. Sci.* **47**: 929–950.
- Tulloch R, Smith KS. 2006. A theory for the atmospheric energy spectrum: Depth-limited temperature anomalies at the tropopause. *Proc. Natl. Acad. Sci. USA* **103**: 690–694.